# INVESTIGATION INTO ELECTRON CLOUD EFFECTS IN THE ILC DAMPING RING DESIGN[*]

J.A. Crittenden, J. Conway, G.F. Dugan, M.A. Palmer, D.L. Rubin, J. Shanks, K.G. Sonnad
*CLASSE, Cornell University, Ithaca, NY 14853, USA*

L. Boon, K. Harkay
*ANL, Argonne, IL 60439, USA*

M.A. Furman
*LBNL, Berkeley, CA 94720, USA*

S. Guiducci
*LNF, Frascati, Italy*

M.T.F. Pivi, L. Wang
*SLAC, Menlo Park, CA 94025, USA*
(Dated: October 7, 2013)

We report modeling results for electron cloud buildup and instability in the International Linear Collider positron damping ring lattice design. Updated optics, wiggler magnets, and vacuum chamber designs have recently been developed for the 5 GeV, 3.2-km racetrack layout. An analysis of the synchrotron radiation profile around the ring has been performed, including the effects of diffuse and specular photon scattering on the interior surfaces of the vacuum chamber. The results provide input to the cloud buildup simulations for the various magnetic field regions of the ring. The modeled cloud densities thus obtained are used in the instability threshold calculations. We conclude that the mitigation techniques employed in this model will suffice to allow operation of the damping ring at the design operational specifications.

## I. INTRODUCTION

The discoveries at the Large Hadron Collider [1, 2] have re-intensified interest in the proposed International Linear Collider (ILC) [3]. Operation of the ILC depends critically on the reliable performance of the electron and positron damping rings (DRs) employed as injectors. Electron cloud (EC) buildup has been shown to limit the performance of positron storage rings at KEK-B [4] and PEP-II [5]. For the past several years, we have been developing and validating modeling codes for the purpose of designing the ILC DRs. This paper presents the results of those efforts. We present the beam optics design, the vacuum chamber designs including the chosen cloud buildup mitigation techniques, cloud buildup simulations and modeled estimates of instability thresholds, deriving conclusions on the feasibility of building and operating the positron DR to specification.

## II. DESIGN OF THE POSITRON DAMPING RING LATTICE

The racetrack layout for the 3238-m circumference ILC damping is described in the ILC Technical Design Report [**? **]. The 100-m-long RF straight can accommodate as many as 16 single-cell cavities and the 226-m wiggler straight up to 60 superferric wigglers [6]. The baseline design (26-ms damping time and 5-Hz operation) requires 8 cavities with total accelerating voltage of 14 MV and 54 2.1-m-long wigglers with 1.51-T peak field. In order to run in the proposed 10-Hz mode, the wigglers operate at 2.16 T to cut the radiation damping time in half, and the accelerating voltage is increased to 22.4 MV with 12 cavities to preserve the 6-mm bunch length. The 339-m phase trombone occupies the same straight as the wigglers and consists of five six-quadrupole cells and has a tuning range of $\pm 0.5$ betatron wavelengths. The opposite straight includes injection and extraction lines, and the 117-m-long chicane for fine adjustment of the revolution period. The range of the chicane is $\pm 4.5$ mm with negligible contribution to the horizontal emittance. The arc cell is a simple variation of a TME-style cell with a single 3-m bend, three quadrupoles, one focusing and two defocusing, for a total length of 9.7 m. There are 75 cells in each arc. The dynamic aperture including magnet multipole errors and misalignments, and wiggler nonlinearities, is large enough to accept the phase space of the injected positrons, defined so that the normalized horizontal and vertical emittances $A_x$ and $A_y$ satisfy $A_x + A_y < 0.07$ m-rad and $\Delta E/E \leq 0.075\%$ [7].

FIG. 1.



FIG. 2.



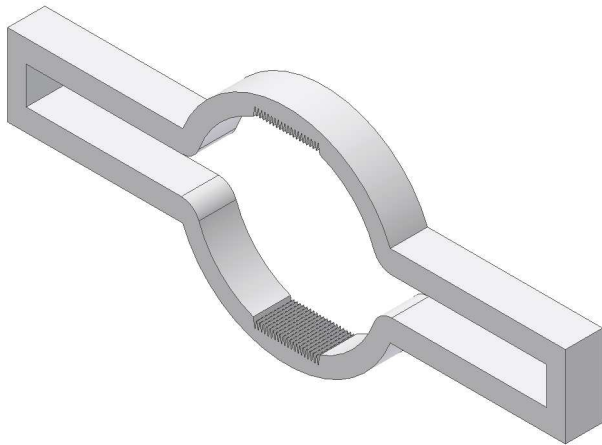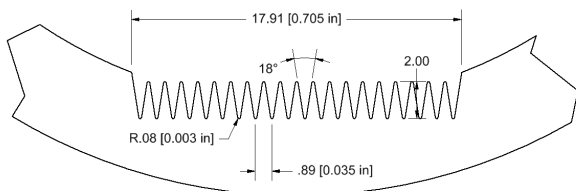FIG. 3.



FIG. 4.

## III.  VACUUM CHAMBER DESIGN

The conceptual design of the vacuum chambers incorporates mitigation techniques in each of the various magnetic field environments to suppress the local buildup of the EC. The mitigation methods were selected based on the results of an intense research effort conducted as part of the ILC Technical Design program [8]. The vacuum system conceptual design is described in Ref. [9]. In the arc regions of the ring, the 50-mm aperture vacuum chambers utilize TiN-coating to suppress the secondary electron yield (SEY) of the chambers, and dual antechambers to reduce the number of photoelectrons entering the central region. The rear walls of the antechambers are angled as well. In the dipoles, the EC is further suppressed by the use of longitudinal grooves on the top and bottom surfaces, as shown in Figs. 1 and 2.  In the wiggler region, a 46-mm aperture chamber utilizes clearing electrodes (see Figs. 3 and 4) to suppress growth of the cloud and dual antechambers along with custom photon stops to suppress the generation of photoelectrons.

In the straights of the dogleg ring, the 50-mm aperture round vacuum chamber is TiN-coated for secondary suppression. Drift regions throughout the ring will employ solenoid windings to further suppress cloud buildup near the beam.
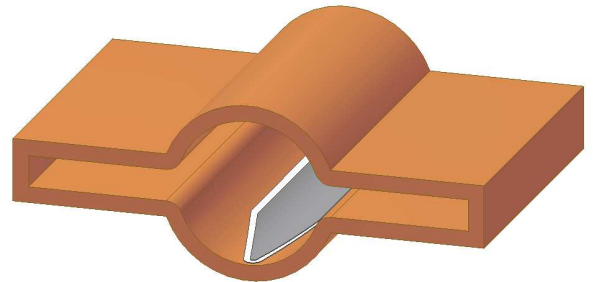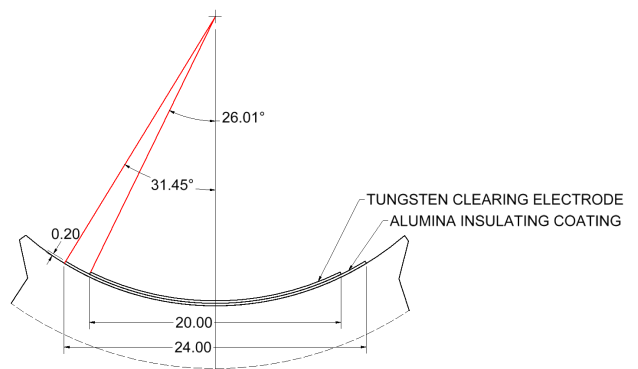
## IV.  PHOTON TRANSPORT MODEL

The distribution of synchrotron radiation photon absorption sites around the ring can be used to predict the sources of the photoelectrons which seed the EC. This distribution has been computed for the DTC03 lattice using a newly developed photon-tracking simulation code, Synrad3D [10]. This code computes the synchrotron radiation photons per electron generated by a beam circulating in the magnetic lattice, and simulates the propagation in three dimensions, of the photons as they scatter off, or are absorbed by, the vacuum chamber. The design vacuum chamber geometry, including details such as antechambers and photon stops, is used in the calculation. Both specular and diffuse photon scattering are included in the simulation. For the scattering calculation, the surface material is approximated as aluminum with a thin carbon coating, and the surface parameters are representative of a typical technical vacuum chamber, namely rms roughness 100 nm and correlation length 5000 nm.

Figure 5 shows the photon intensity distributions for magnetic elements in one of the arcs of the DR. The low photon rates at zero and $\pi$ radians are due to the antechambers. The top-bottom asymmetry is due to a non-vertical slope introduced in the antechamber back walls to inhibit scattering out of the antechamber.
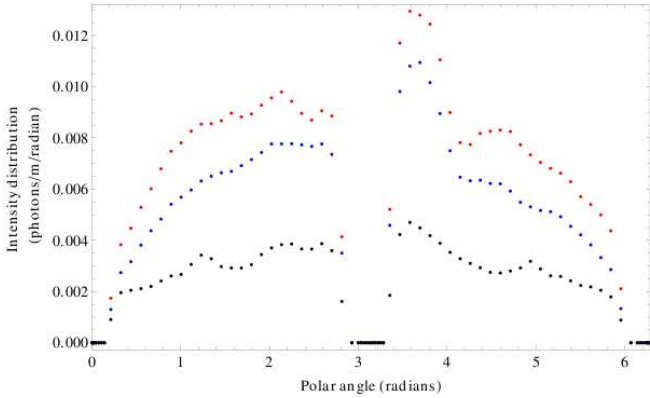
FIG. 5. Intensity distributions for absorbed photons in one arc of the DR, averaged over three types of magnetic environments. The average over the quadrupole regions is shown in red. The average over the field-free regions is shown in blue and the average over the dipole regions is shown in black. The angle is defined to be zero where the vacuum chamber intersects the bend plane on the outside of the ring. The angle $\pi/2$ corresponds to the top of the vacuum chamber.

## V. EC BUILDUP IN THE ARC DIPOLES

Using the code POSINST [11], we have simulated the EC buildup in the arc dipoles under the following assumptions: 1) the most relevant SEY model parameters are those obtained from fits to measurements obtained Cornell Electron Storage Ring Test Accelerator (CESRTA) project [12] for a TiN surface [13], 2) the distribution of photons striking the chamber surface at the location of the dipole magnet has been obtained from Synrad3D calculations, and 3) the quantum efficiency is 0.05, independent of photon energy and incident angle.

The SEY model corresponding to the above-mentioned fits yields a peak SEY value of 0.94 at an incident electron energy of 296 eV. In addition to this, we have carried out the simulation in which the SEY is set to 0 (meaning that any electron hitting the chamber walls gets absorbed with unit probability) in order to isolate the contribution to the EC density $N_e$ from photoemission.

A similar simulation for the earlier DSB3 lattice [14] was made under somewhat different assumptions regarding photoemission and secondary emission. Specifically, the quantum efficiency was assumed to be 0.1, the incident photon distribution was assumed to be a simple superposition of a flat background plus a Gaussian at the photon impact point, and the SEY model was obtained from older fits to other samples and re-scaled so that the peak SEY was assumed to be 1.0. We recently repeated this simulation for DSB3 under the assumption that the quantum efficiency is 0.05, without changing any other parameters. The results for the DTC03 lattice and the new results for the DSB3 lattice are summarized in Table I. Cloud densities averaged over the full vacuum chamber as well as those averaged over a $20\sigma_x \times 20\sigma_y$ elliptical cross-sectional area are shown. These modeling

statistical uncertainties are at the level of less than 30%. To summarize: 1) the cloud density $N_e$ in an arc dipole

TABLE I. POSINST modeling results for EC densities $N_e$ ($10^{11}$ m$^{-3}$) in the dipole regions of the DTC03 and DSB3 lattices. The first row shows the density at the end of a 34-bunch train. The second rows shows the peak 20-$\sigma$ density during the train. The third row gives the maximum 20-$\sigma$ density just prior to the arrival of a bunch.

|  | DSB3 | | DTC03 | |
| --- | --- | --- | --- | --- |
|  | SEY=0 | SEY=1.0 | SEY=0 | SEY=0.94 |
| 34-bunch density | $\sim 0.2$ | $\sim 0.4$ | $\sim 0.5$ | $\sim 1.2$ |
| Peak 20-$\sigma$ density | $\sim 0.1$ | $\sim 0.2$ | $\sim 0.2$ | $\sim 0.5$ |
| 20-$\sigma$ density prior to bunch arrival | $\sim 0.1$ | $\sim 0.2$ | $\sim 0.2$ | $\sim 0.4$ |

for DTC03 is roughly twice that for DSB3, 2) this factor of about two is a direct consequence of the doubling of the photoemission rate for DTC03 relative to DSB3, 3) the factor of two holds whether the peak SEY is 0 or 0.94, 4) the results for peak SEY=0 (no secondary electrons) amount to a lower limit on $N_e$, 5) however, one must keep in mind that this lower limit is directly proportional to the quantum efficiency, assumed here to be 0.05, 6) for peak SEY=0.94, $N_e$ is a factor of 2 or 3 greater than that for SEY=0, both for DSB3 and DTC03, 7) these results for peak SEY=0.94 represent an upper limit for those expected for a grooved surface, 8) the $20\sigma$-density is somewhat smaller than the above-quoted overall average $N_e$, and 9) the same is true for the $20\sigma$-density prior to bunch passage.

## VI. EC BUILDUP IN THE QUADRUPOLES, SEXTUPOLES AND FIELD-FREE REGIONS

The EC buildup modeling code ECLOUD served to calculate estimates of the cloud densities in the quadrupoles and sextupoles in the arc and wiggler regions and in the field-free regions of the wiggler sections for the DTC03 lattice. The photon transport modeling code Synrad3D provided azimuthal photon absorption distributions average over each of these regions. The POSINST photoelectron production and SEY model parameters were also used in ECLOUD. Representative field strengths of 10 T/m (70 T/m$^2$ )were used for the quadrupoles (sextupoles). Trapping effects were evident in the beam-pipe-averaged cloud densities, which had not yet reached equilibrium during the eight trains simulated, but since the trapping does not occur in the central beam region, the $20\sigma$ densities prior to the passage of each bunch were stable after just a couple of trains. Table II shows the $20\sigma$ density estimates obtained assuming a peak SEY value of 0.94. The POSINST results for the arc dipoles are included in this table. The integrated ring lengths for the magnetic environment types are also shown. The simulations for the field-free regions were repeated imposing a solenoidal magnetic field of 40 G, as is

TABLE II. POSINST and ECLOUD modeling results for the $20\sigma$ density estimates $N_e$ ($10^{11}$ m$^{-3}$) just prior to each bunch passage in the DTC03 lattice design. The total length of each magnetic field environment $L$ is given in meters.

| | Field-free | | Dipole | | Quadrupole | | Sextupole | |
|---|---|---|---|---|---|---|---|---|
| | L | $N_e$ | L | $N_e$ | L | $N_e$ | L | $N_e$ |
| Arc region 1 | 406 | 2.5 | 229 | 0.4 | 146 | 1.5 | 90 | 1.4 |
| Arc region 2 | 365 | 2.5 | 225 | 0.4 | 143 | 1.7 | 90 | 1.3 |
| Wiggler region | 91 | 40 | 0 | | 18 | 12 | 0 | |

foreseen in the mitigation recommendations determined during the ECLOUD10 workshop [8]. Such a field was shown to reduce the cloud buildup in the beam region to negligible levels.

## VII. EC BUILDUP IN THE WIGGLERS

The EC build-up in the wiggler is simulated using the CLOUDLAND code. The ring length occupied by wigglers is 118 m. The most relevant SEY parameters are those obtained from fits to the data obtained from the PEP-II storage rings [? ]. The simulation assumes a peak SEY of 1.2 for the copper surface of a wiggler chamber. The energy at the peak SEY is 250 eV. The photon flux used in the simulation is 0.198 photon/m/positron and a uniform azimuth distribution is assumed. A quantum efficiency of 0.1 and a beam size $\sigma_x/\sigma_y = 80\mu/5.5\mu$ was used in the simulation. The peak wiggler field is 2.1 T. The beam chamber of the wiggler section includes an antechamber with 1 cm vertical aperture. A round chamber with diameter of 46 mm is used, which is a good approximation since most electrons accumulate near the horizontal center due to multipacting. The CLOUDLAND calculation shows that a beam with bunch population of $2\times10^{10}$ and bunch spacing of 6 ns can excite strong multiplication near the horizontal center. The peak electron density seen by the last bunch along the bunch train is about $1.2\times10^{13}$ m$^{-3}$ The wiggler vacuum design foresees the inclusion of clearing electrodes. The curved electrode with width of 20 mm is located on the bottom of the chamber. The simulations described below included this electrode design. The SEY parameters for the electrode were assumed to be the same as those for the chamber surface. The actual electrode design has thermal spray tungsten and Alumina insulator. It was found that a positive electrode bias is extremely effective at suppressing multipacting. A positive voltage of a few hundred volts suffices. Interestingly, the suppression effect is not necessarily a monotonic function of the clearing voltage. The complication of the dynamics of electrons due to the clearing field, beam field and space-charge field results in this non-monotonic dependence. A weak positive voltage makes a very low electron density area with the same horizontal width as the electrode. The suppression of the cloud is effective only over the horizontal region covered by the electrode.
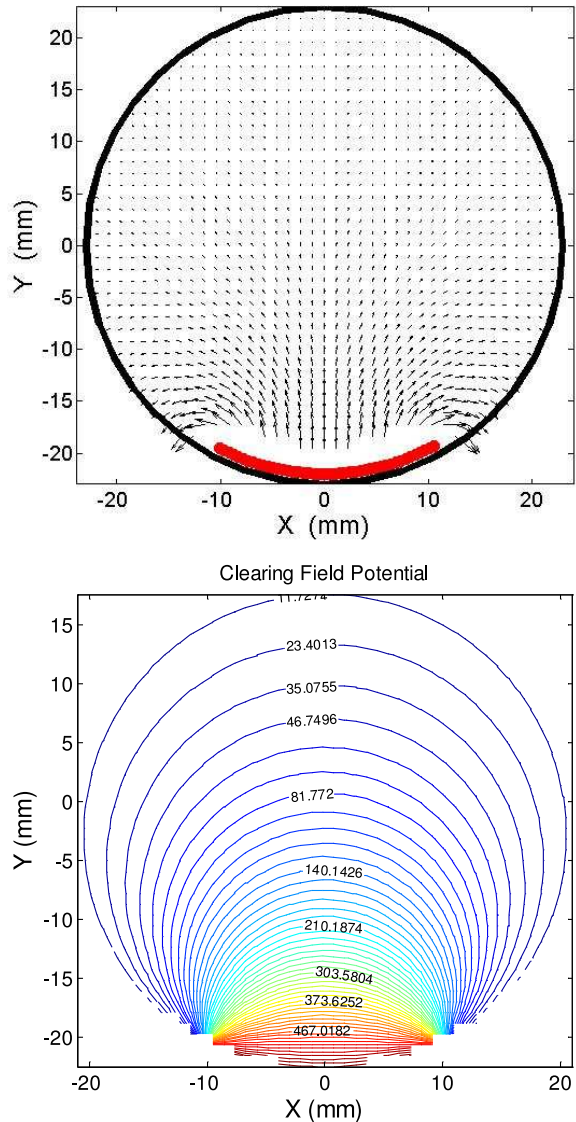


FIG. 6. The clearing electrode in the round chamber used in the wiggler magnet. The clearing field vectors are shown above and the equipotential lines are shown in the lower plot.

### A. from presentation Lanfa Wang

Simulation Parameters

- Peak SEY = 1.2
- Energy at peak SEY = 250 eV
- Photon reflectivity = 100%
- Photon flux = 0.198 $\gamma$/m/positron
- $\sigma_x/\sigma_y$ of beam = 80 $\mu$m/5.5 $\mu$m
- Bunch population = $2\times10^{10}$
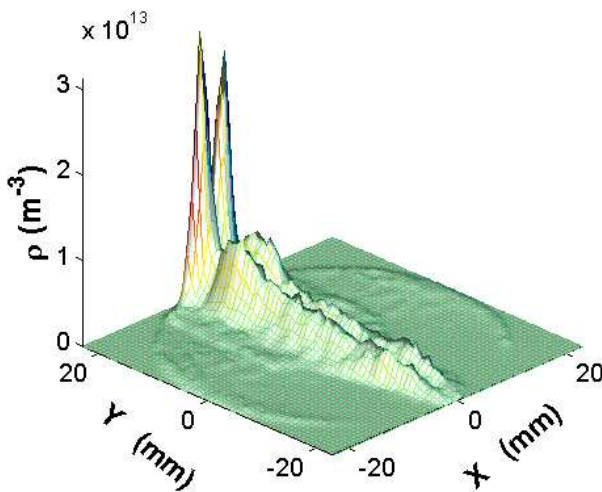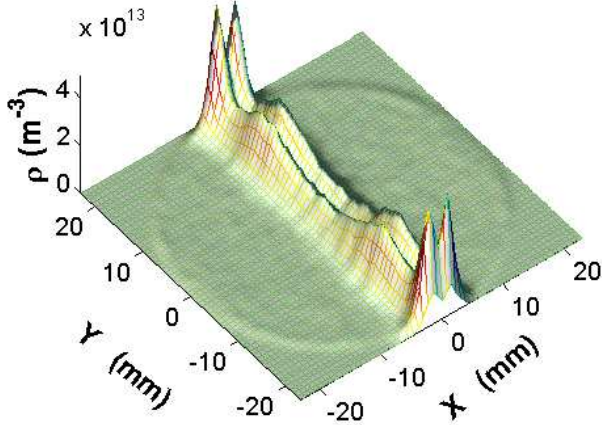- Peak wiggler field = 2.1 T

FIG. 7.



FIG. 8.

- Bunch spacing : 6.15 ns

- Beam filling pattern: 34 bunches/per train followed by a gap of 45 RF buckets

- Electrode Voltage: varies from -600 V to +600 V

With negative voltages

- Electrodes helps, however, it less effective comparing with positive voltages

- The effect is not necessarily monotonic. (For instance, -200 V is better than -300 V at the beginning)
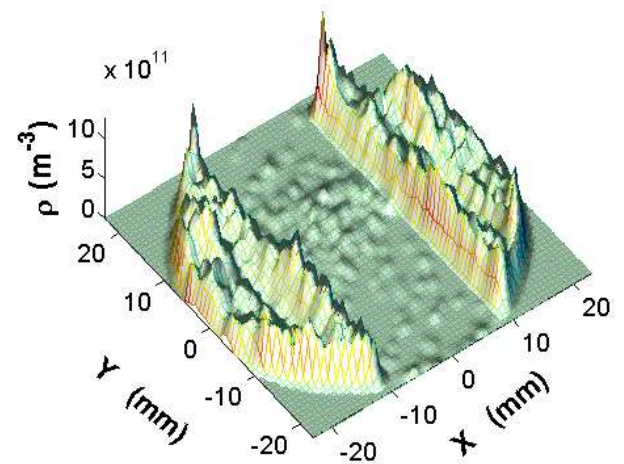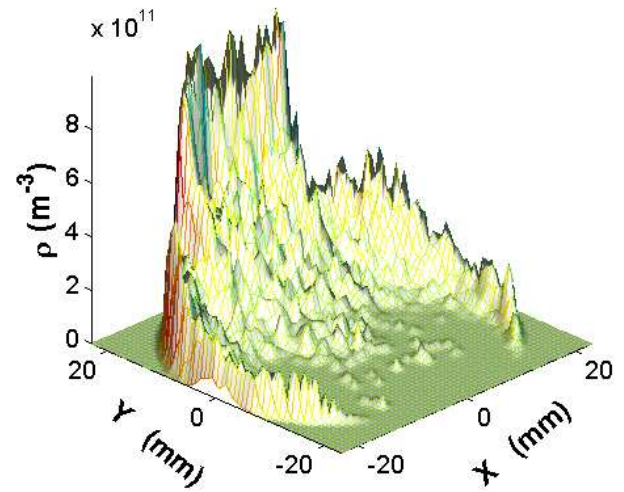
With Positive voltages

- Electrodes with a positive voltages (relative to the ground, which is the chamber here) is very effective

- 100 V is good enough, even better! There are no much difference for a voltage ranges from 300 V 600 V

- Note there is only a few macro-particles near the beam, therefore, the density near the beam is very noisy. The density see by the positron beam is below 1.0e10/m3, although the average density is below 1.0e10/m3 level.

FIG. 9.



FIG. 10. Effect of the clearing electrode with negative voltages in the wiggler chambers. (a) Average e-cloud density (b) e-cloud density near the beam

beam bunches. The dipole simulations are to be considered conservative, since the effect of the grooves was not included in the density calculations.
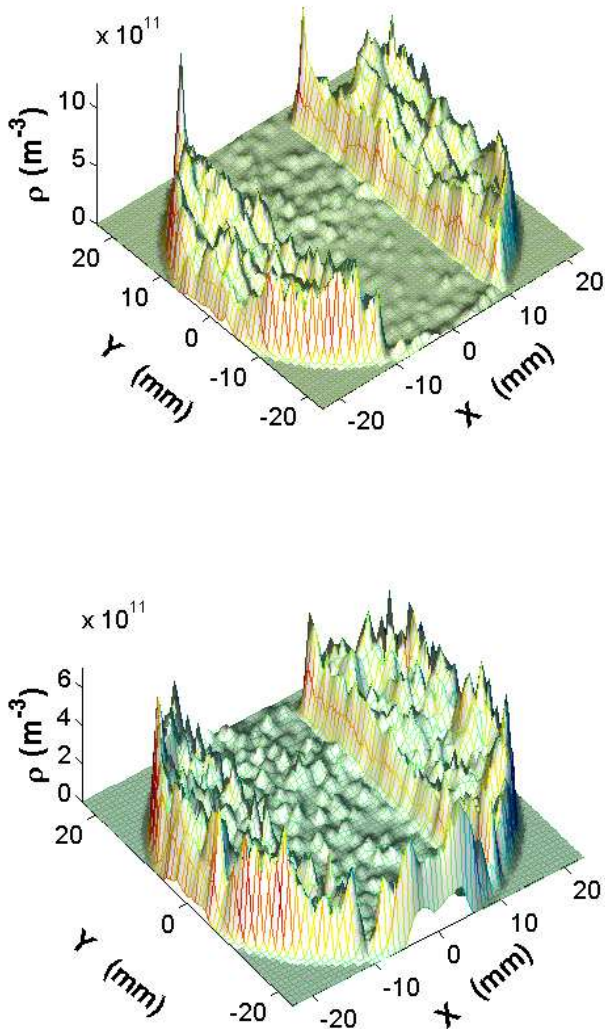
## VIII.   FUTURE WORK

The modeling work on EC buildup described above provides estimates of the cloud density in the region of the beam at the time of a bunch passage. The estimates are encouraging, placing an upper limit on the ring-averaged density of about $3.5 \times 10^{10}$ m$^{-3}$, about a factor of three lower than assumed in earlier instability simulations, which did not account for all the mitigation techniques included here.. The additional suppression provided by the grooved surfaces recommended for the arc dipole regions remains to be calculated for the DTC03 lattice [15, 16]. Based on these results, the simulation code CMAD [17] has been used to estimate single-bunch instabilities arising due to the effect of the cloud on the
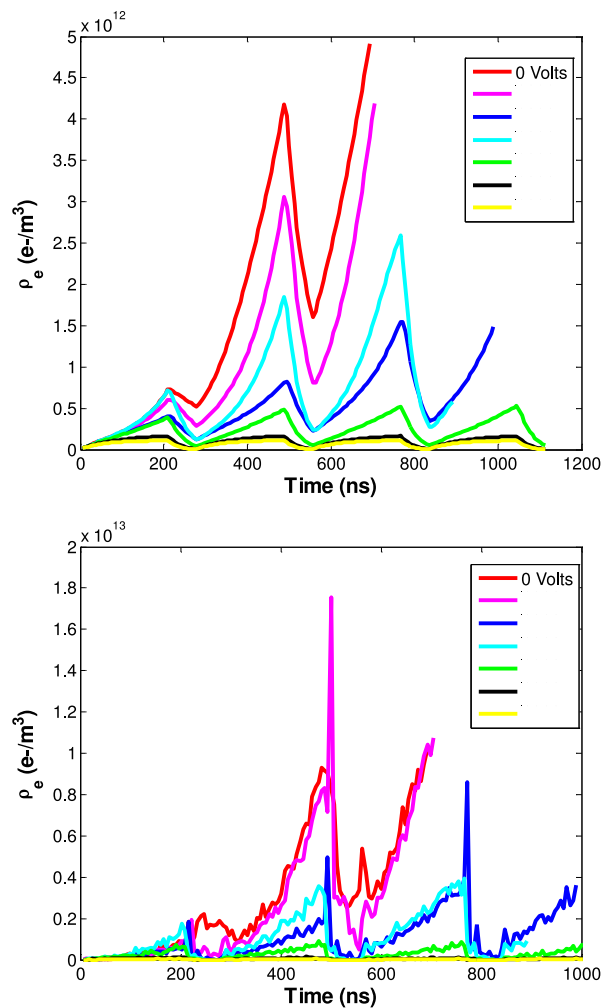
## IX.   BEAM DYNAMICS SIMULATION

The dilution of the vertical emittance is the primary concern of EC effects in DRs. To estimate the beam emittance growth caused by ECs, the beam dynamics simulation program CMAD [17] was used. The parameters used to perform these simulations were based on the lattice design and the estimates of the cloud densities obtained from build up simulations mentioned in the previous sections. The study was performed in two separate phases that each account for different modeling of the damping time. The first involved a smooth focusing model, which was followed by a configuration that involved the full lattice of the DR. The smooth focusing model is highly
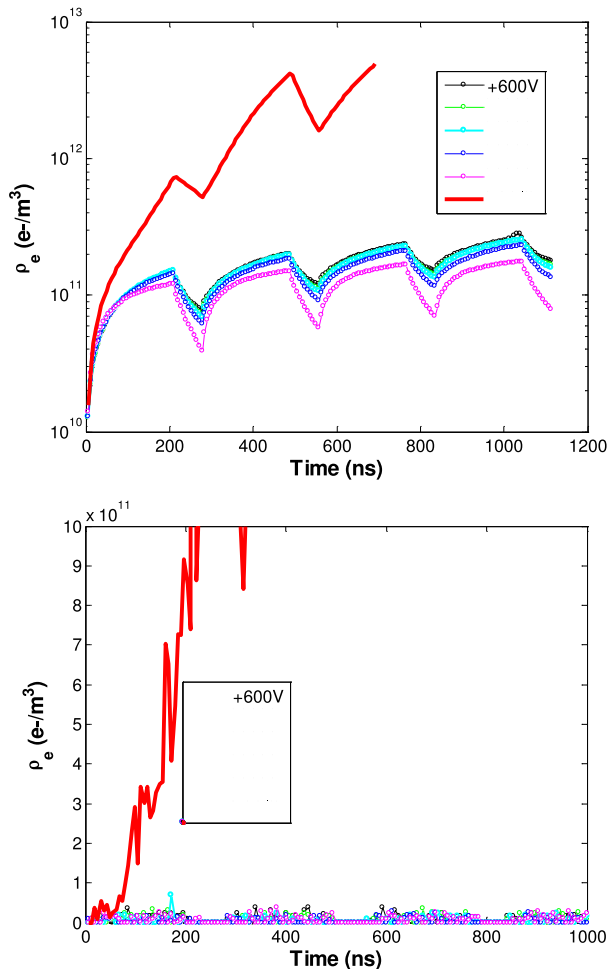
FIG. 11. Effect of the clearing electrode with positive voltages in the wiggler chambers. (a) Average e-cloud density (b) e-cloud density near the beam

| Beam energy | 5 GeV |
|---|---|
| Unnorm. emittance x, y | 0.5676 nm, 2.0 pm |
| Bunch population | $2 \times 10^{10}$ |
| Bunch length | 0.6036 cm |
| Tunes x, y, z | 48.248, 26.63, 0.0314 |
| Momentum compaction | $3.301 \times 10^{-3}$ |
| Circumference | 3234.3540 m |
| Energy Spread | $1.1 \times 10^{-3}$ |
| Chromaticity x,y | 1.0 dQ/d(dp/p) |

TABLE III. List of physical parameters used in the CMAD simulations, corresponding to the DTC03 lattice design

| Macro e+ | 300000 |
|---|---|
| Macro e- | 100000 |
| Bunch slices | 96 |
| Grid nodes | $128 \times 128$ |
| Domain extent x, y | 20 sigma |
| Domain extent z | +/- 2 sigma |
| IPs (fixed $\beta$ only)) | 400 |
| Nr parallel processors | 96 |

TABLE IV. List of computational parameters used in the CMAD simulations. The number of IPs is used only in the smooth-focusing model

simplified but is far more efficient in performing computations. This model was used to scan through a set of cloud densities in order to estimate the range over which the behavior transitions from a gradual and linear to a fast exponential growth in emittance. It should be noted effects of damping and diffusion due to synchrotron radiation emission are not included in the calculations. The effects of radiation damping and quantum excitation are both slower than the instability growth time.

The working of CMAD is similar to some other programs such as HEADTAIL [18], WARP [19] and PHETS [20]. Results from CMAD, HEADTAIL and WARP have been validated against each other for the the smooth focusing case [21] and the lattice case [22]. The smooth focusing model uses a constant beta function value that is obtained from the betatron tunes and the circumference. The model has no dispersion. As a result there is no variation of the beam size based on the position in the ring. The model uses discrete beam-cloud interaction points (IPs) located at discrete points in the

ring. It is important that the number of IPs exceeds the value of the absolute betatron tune. This ensures that there is sufficient sampling of phases, which is important to avoid artificial resonances arising from the discreteness of beam-cloud interaction.

The details of the physical and computational parameters are given in tables IX and IX respectively. The chromaticity in the lattice was not part of the original design. The value chosen was typical of what accelerators such as CESRTA operate at. Beam dynamics simulations require that the chromaticity be set to a reasonable value to ensure stability introduced by "chromatic damping". The computational parameters were chosen based on experience in simulating cases for CESRTA [23, 24]. The computational domain was truncated at 20 rms beam sizes in the transverse directions and at 2 rms beam sizes in either direction for the longitudinal extent. The large transverse extent ensures that enough of the EC that is affecting the beam during the pinching process is accounted for. The number of IPs used in the smooth focusing model was 400 which was well above the number of betatron oscillations per revolution, or the tunes which are given in table[IX. The beam was sliced longitudinally into 96 segments and the computation was performed in parallel, distributed over 96 processors.

Figure 12 shows the emittance growth over a period of 500 turns using the smooth focusing model. The simulations were done over a wide range of EC densities. Figure 12a) shows the emittance growth rate for three cases, with the intermediate cloud density of $3.5 \times 10^{10} m^{-3}$ corresponding to the estimated average cloud density over the ring after applying all the mitigation methods mentioned in the previous sections. Figure 12b) shows that
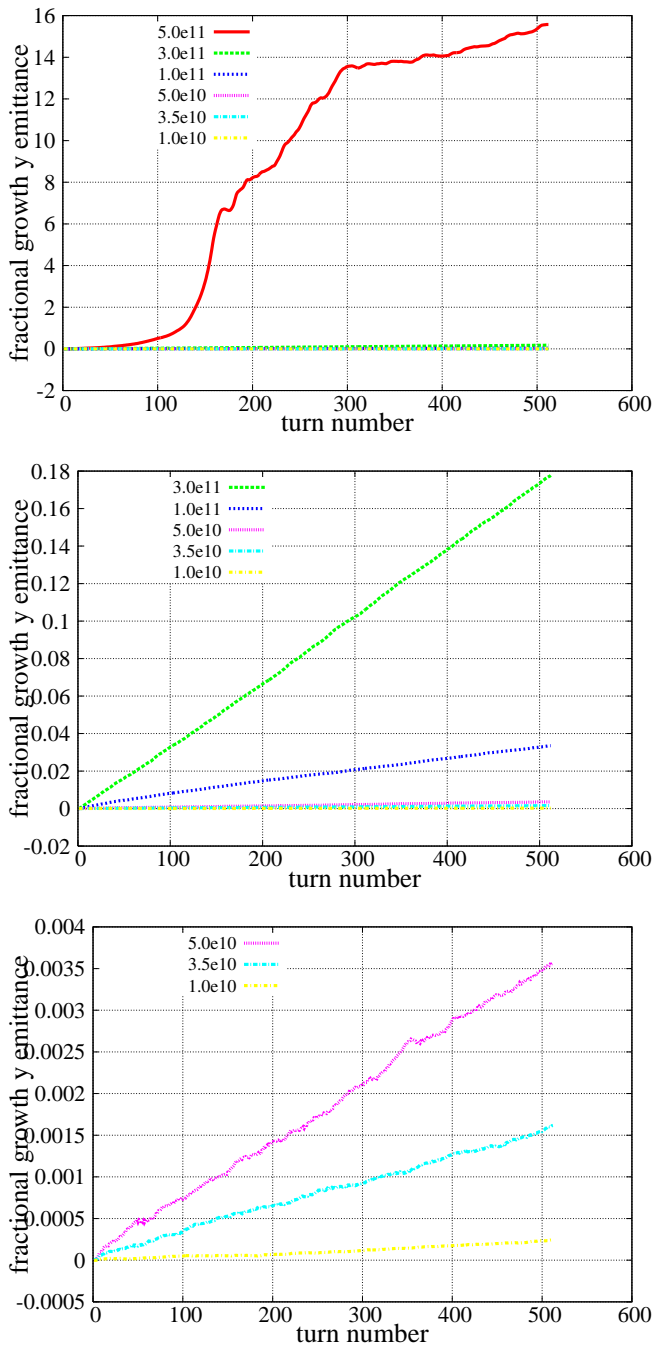
FIG. 12. Calculation of vertical emittance growth using the continuous focusing model for varying cloud densities

| Element | Cloud density | % occupancy |
|---|---|---|
| drifts | 0e10 | 66 |
| bends | 4.e10 | 15.14 |
| Quads in arcs | 0.16e12 | 9.8 |
| Sextupoles in arcs | 0.135e12 | 5.56 |
| wigglers | 1.5e10 | 2.961934 |
| Quads in wiggler region | 1.2e12 | 0.49 |
| average | 3.5e10 | |

TABLE V. Cloud density in various element and their respective occupancy factors

sure that the accelerator operating point is well below this value. These results shows the cloud density is expected to be about a factor of ten below the transition point.

In a second simulation phase, a similar estimate of emittance growth was done using the full lattice of the DR design. In this case the beam particles were transported using first order $6 \times 6$ transfer matrices. This includes variation of the horizontal and vertical beam size with beta function and dispersion. In particular, the beam size ratio $\sigma_x/\sigma_y$ reached a value of about 100, imposing challenging numerical accuracy conditions. The beam underwent an interaction with the EC at each element in the lattice. Thus the number of IPs used in this case was 5765, equal to the number of elements in the lattice design model. The wigglers were modeled using a bend-drift-bend sequence. In these simulations, of the segment had an external dipole field (Kiran, need explanation here), the electron was moved based on the Lorentz force applied to the particle. The cloud density was different in each element, based on the build up simulations performed for the individual elements under the given beam conditions. These densities are listed in table[IX]. Thus, several physical details omitted from the continuous focusing model were taken into account in these simulations.

the vertical emittance growth rate increases almost by two orders of magnitude when the cloud density increases by about a factor of 10. Figure 12c) includes a case where the growth rate transitions from linear to exponential. The linear region below the "instability threshold" is fairly typical and has been observed in previous single-bunch simulations with other modeling codes. It is important to understand the point at which this transition to exponential behavior takes place in order to en-
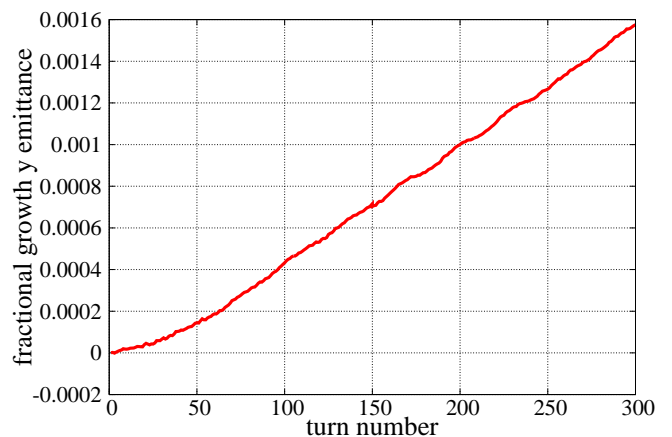


FIG. 13. Estimate of the emittance growth using the full lattice in the model with specified cloud densities in each element of the lattice

Figure 13 shows the evolution of the beam emittance under the EC conditions given in Tab. IX. The result shows that the fractional emittance growth over 300 turns is 0.0016. Except for an initial transient phase in the first 25 turns, the growth is linear all along. The ILC DR beam store time is 18550 turns. Thus, in the absence of any damping mechanism over this time period, one can expect that the beam emittance would increase by 10% (double-check this value) due to ECs at the end of its course in the DR. It should be noted that if the same extrapolation was applied using the continuous focusing case result corresponding to a cloud density of $3.5 \times 10^{10} m^{-3}$, we obtain a growth of 5% (double-check this value) in beam emittance after 18550 turns.

[1] A. Colaboration, Phys. Rev. **B716**, 1 (2012).

[2] C. Colaboration, Phys. Rev. **B716**, 30 (2012).

[3] T. B. et al., *The International Linear Collider Technical Design Report - Volume 1: Executive Summary*, Tech. Rep. arXiv:1306:6327 (arXiv, Cornell University Library, Ithaca, NY, 2013).

[4] .

[5] M. A. Furman and G. R. Lambertson, in *Proceedings of MBI97: International Workshop on Multibunch Instabilities in Future Electron and Positron Accelerators, Tsukuba, Japan, 1997*, KEK Proceedings 97-17, edited by Y. H. Chin (1997) p. 170.

[6] J. A. Crittenden, M. A. Palmer, and D. L. Rubin, in *Proceedings of the 2012 International Particle Accelerator Conference, New Orleans, LA* (2012) pp. 1969–1971.

[7] J. Shanks, D. L. Rubin, J. Crittenden, and M. Palmer, in *Proceedings of the 2012 International Particle Accelerator Conference, New Orleans, LA* (2012) pp. 1972–1974.

[8] M. Pivi and *et al.*, Proceedings of IPAC2011 , TUPC030 (2011).

[9] J. Conway, Y. Li, and M. Palmer, *Proceedings of the 2012 International Particle Accelerator Conference, New Orleans, LA*, , 1960 (2012).

[10] G. Dugan and D. Sagan, Proceedings of the 49th ICFA Advanced Beam Dynamics Workshop.

[11] M. A. Furman and M. T. F. Pivi, Phys. Rev. ST Accel. Beams **5**, 124404 (2002), 10.1103/PhysRevSTAB.5.124404.

[12] G. F. Dugan, M. A. Palmer, and D. L. Rubin, in *ICFA Beam Dynamics Newsletter*, No. 50, edited by J. Urakawa (International Committee on Future Accelerators, 2009) pp. 11–33.

[13] J. Kim, D. Asner, J. Conway, S. Greenwald, Y. Li, V. Medjidzade, T. Moore, M. Palmer, and C. Strohman, in *Proceedings of the 2011 Particle Accelerator Conference, New York, NY* (2011) pp. 1253–1255.

[14] M. Furman, LBNL-4474E/CBP-874 (2010).

[15] L. Wang and *et al.*, proceedings of PAC07 , FRPMS079 (2007).

[16] M. Venturini and *et al.*, proceedings of PAC07 , THPMN118 (2007).

[17] M. Pivi, Proceedings of PAC07, Albuquerque, New Mexico, USA (2007).

[18] G. Rumolo and F. Zimmermann, Phys. Rev. ST Accel. Beams **5**, 121002 (2002).

[19] J.-L. Vay, A. Friedman, and D. P. Grote, Proceeding of the 9th International Computational Accelerator Physics Conference **1**, 262.

[20] K. Ohmi, Proceedings of the 2001 Particle Accelerator Conference, Chicago , 1895 (2001).

[21] J.-L. Vay and *et al*, Proceedings of PAC09, Vancouver, BC, Canada (2009).

[22] K. G. Sonnad and *et al*, Proceedings of ECloud 2010, Ithaca NY (2010).

[23] K. G. Sonnad and *et al*, Proceedings of 2011 Particle Accelerator Conference, New York, NY, USA , WEP109 (2011).

[24] K. G. Sonnad and *et al*, Proceedings of IPAC2011, San Sebastin, Spain , MOPS084 (2011).

[25] C. A. et al., *The International Linear Collider Technical Design Report - Volume 3: Accelerator Baseline Design*, Tech. Rep. arXiv:1306:6328 (arXiv, Cornell University Library, Ithaca, NY, 2013).

[26] M. T. F. Pivi, J. S. T. Ng, F. Cooper, D. Kharakh, F. King, R. E. Kirby, B. Kuekan, C. M. Spencer, T. O. Raubenheimer, and L. F. Wang, Nucl. Instrum. Methods Phys. Res. **A621**, 33 (2010).